

Paths to caustic formation in turbulent aerosols

Jan Meibohm,¹ Vikash Pandey,² Akshay Bhatnagar,³ Kristian Gustavsson,¹ Dhruvadya Mitra,³ Prasad Perlekar,² and Bernhard Mehlig¹

¹*Department of Physics, Gothenburg University, SE-41296 Gothenburg, Sweden*

²*TIFR Centre for Interdisciplinary Sciences, Tata Institute of Fundamental Research, Gopanally, Hyderabad 500046, India*

³*NORDITA, Royal Institute of Technology and Stockholm University, Roslagstullsbacken 23, SE-10691 Stockholm, Sweden*

The dynamics of small, yet heavy, identical particles in turbulence exhibits singularities, called caustics, that lead to large fluctuations in the spatial particle-number density, and in collision velocities. For large particle, inertia the fluid velocity at the particle position is essentially a white-noise signal and caustic formation is analogous to Kramers escape. Here we show that caustic formation at small particle inertia is different. Caustics tend to form in the vicinity of particle trajectories that experience a specific history of fluid-velocity gradients, characterised by low vorticity and a violent strain exceeding a large threshold. We develop a theory that explains our findings in terms of an optimal path to caustic formation that is approached in the small inertia limit.

Ensembles of heavy particles in turbulence, such as water droplets in turbulent clouds [1] or dust grains in the turbulent gas of protoplanetary disks [2, 3], may exhibit large fluctuations of the particle-number density and of their relative velocities [4–7]. These fluctuations are enhanced by the formation of caustics [8–10], i.e., folds of the particle distribution over configuration space. Caustic formation is an effect of particle inertia, driven by the fluid-velocity gradients, that gives rise to a multi-valued particle-velocity field. Due to this multivaluedness, often called the ‘sling effect’ [11, 12], particles may approach each other, and possibly collide, at large relative velocities. Accordingly, caustics have an important impact on the distribution of relative velocities [13–16], and are a crucial ingredient to theories for collision rates and collision outcomes [17–19]. In effect, caustic formation may increase the variance of the particle size distribution in turbulent aerosols because, on the one hand, caustics facilitate particle growth by enhancing collision rates [14, 16]. Increased collision velocities may, on the other hand, lead to fragmentation, and thus to reduced particle sizes [3].

Caustics have been extensively studied in direct numerical simulations (DNSs) of particles in turbulence [12] and model flows [9, 20–25]. Recent numerical studies [26, 27] found that high-velocity collisions tend to occur where the turbulent strain is large, but this cannot be explained in terms of the white-noise models usually used to study caustic formation [8–10]. A precise understanding of how caustics form at small particle inertia, including the local flow conditions that lead to their formation, is crucial for the identification of caustics in experiments [28] and for sampling them efficiently in DNS [12].

In this Letter, we describe a significant step towards a detailed understanding of how caustics form in turbulence. Using a DNS of two-dimensional turbulence, we show that whether a caustic forms or not depends on the history of the fluid-velocity gradients experienced by closeby particles, not just upon instantaneous correlations between particle positions and flow gradients (pref-

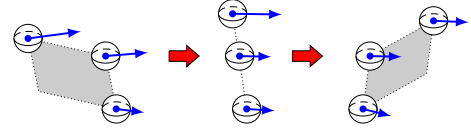


FIG. 1. Illustration of caustic formation in two spatial dimensions. Shown are three nearby particles. A caustic is formed when faster particles overtake slower ones. At a caustic, the area \mathcal{V} of the parallelepiped spanned by separation vectors between the three particles, shown in grey, vanishes.

erential concentration [7, 29, 30]). When particle inertia is small, we find a most likely history, i.e., an “optimal path” to caustic formation. To determine this path is an optimal-fluctuation problem, similar in nature to localisation due to optimal potential fluctuations in disordered conductors [31], population extinction due to environmental and population-size fluctuations [32, 33], and shock formation in Burgers turbulence [34, 35]. Based on this observation, we develop a theory that explains how the strain and vorticity change along the optimal path to caustic formation: The fluid strain performs a time-localised, violent fluctuation that exceeds a large threshold, while vorticity remains small. Our results explain qualitatively why DNSs of particles in turbulence show increased collision rates in straining regions [26, 27]. Even at finite inertia, the optimal path leaves a clear mark in the data, providing criteria for the identification and the efficient sampling of caustics in experiments and in DNSs.

In a dilute suspension of small, heavy, spherical particles, the dynamics of a single particle is approximately given by Stokes’ law [7],

$$\frac{d}{dt}\mathbf{x}(t) = \mathbf{v}(t), \quad \frac{d}{dt}\mathbf{v}(t) = \tau_p^{-1}\{\mathbf{u}[\mathbf{x}(t), t] - \mathbf{v}(t)\}. \quad (1)$$

Here, \mathbf{x} and \mathbf{v} denote particle position and velocity; $\tau_p = 2a^2\rho_p/(9\rho_f\nu)$ is the particle-relaxation time which depends on the particle size a , the kinematic viscosity ν of the fluid, and the particle and fluid densities, ρ_p and ρ_f , respectively. The turbulent fluid-velocity field, evaluated

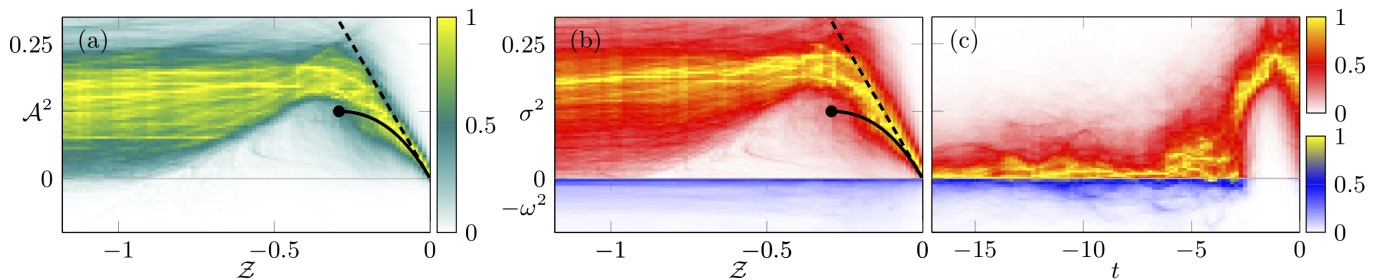


FIG. 2. Path to caustic formation for $St = 0.31$. Numerical results using a DNS of two-dimensional turbulence. The path density is colour coded, normalised to unity along each slice of constant Z to improve visibility. (a) Path density in the Z - \mathcal{A}^2 plane. The dashed line shows the approximation, $Z \sim \mathcal{A}^2$. The solid line shows the evolution of the stable fixed point according to Eq. (6). The dot marks the bifurcation to instability (see main text). (b) Individual contributions from strain (Z vs σ^2 , positive axis) and vorticity (Z vs $-\omega^2$, negative axis). (c) Path densities for σ^2 (positive axis) and $-\omega^2$ (negative axis) as a function of time before caustic formation at $t = 0$.

at the particle position, is denoted by $\mathbf{u}[\mathbf{x}(t), t]$.

To describe caustic formation, we consider the parallelepiped spanned by $d + 1$ nearby particles in d spatial dimensions. How the spatial volume $\hat{\mathcal{V}}(t)$ of this object contracts or expands under the nonlinear dynamics (1) is determined by the spatial Jacobian $J_{ij}[\mathbf{x}(t_0), t] = \partial x_i(t)/\partial x_j(t_0)$, namely, $\hat{\mathcal{V}}(t) = |\det \mathbb{J}(t)|$. Since the dynamics (1) takes place in $2d$ -dimensional phase space, spatial subvolumes $\hat{\mathcal{V}}$ may collapse in finite time, $\hat{\mathcal{V}} \rightarrow 0$, when a caustic forms [7]. Figure 1 shows a typical particle configuration that leads to a caustic in two spatial dimensions. As is well known, caustic formation is closely related to the dynamics of the particle-velocity gradients, which reads, in dimensionless form [7, 11],

$$St \frac{d}{dt} \mathbb{Z}(t) = -\mathbb{Z}(t) - \mathbb{Z}(t)^2 + \mathbb{A}(t), \quad (2)$$

with initial condition $\mathbb{Z}(t_0) = \mathbb{A}(t_0)$. Here, the Stokes number $St = \tau_p/\tau_K$ is a dimensionless measure of particle inertia; $Z_{ij} = \tau_p \partial v_i(t)/\partial x_j(t)$ and $A_{ij} = \tau_p \partial u_i(t)/\partial x_j(t)$ are the dimensionless matrices of particle-velocity gradients and fluid-velocity gradients, respectively. In Eq. (2), time is dedimensionalised by the Kolmogorov time, $\tau_K^2 = \langle \sum_{i,j=1}^2 (\partial u_i/\partial x_j)^2 \rangle_s = \tau_p^2 \langle \text{Tr}(\mathbb{A}\mathbb{A}^T) \rangle_s$, where $\langle \cdot \rangle_s$ denotes a steady-state ensemble average. Here and in the following, we use the abbreviations $\mathbb{Z}(t) = \mathbb{Z}[\mathbf{x}(t), t]$ and $\mathbb{A}(t) = \mathbb{A}[\mathbf{x}(t), t]$. Using (2), one finds [7]

$$\hat{\mathcal{V}}(t) = \hat{\mathcal{V}}(t_0) \exp \int_{t_0}^t ds \mathbb{Z}(s), \quad (3)$$

where $\mathbb{Z} = \text{Tr} \mathbb{Z}$ is the divergence of the field of particle-velocity gradients. Hence, a necessary condition for caustic formation is that \mathbb{Z} escapes to negative infinity.

Apart from the Reynolds number Re that specifies the turbulence intensity, the particle dynamics is determined by the Stokes number St . For small St , particle detachment is characterised by $\mathbb{A} - \mathbb{Z}$, which is typically of the order of St , and thus small. Caustic formation requires the activation of the nonlinear term in Eq. (2) that drives the particle-velocity gradients into a caustic. This, in

turn, requires rare and violent fluctuations of the fluid-velocity gradients \mathbb{A} of the order of unity.

We determine the dominant events that drive caustic formation by measuring the statistics of paths in the joint space of Z and the fluid velocity gradients \mathbb{A} . In isotropic turbulence, the properties of any statistical quantity must be invariant under rotations. In addition to Z , we therefore map out the paths of the invariants obtained from the symmetric (\mathbb{S}) and antisymmetric (\mathbb{O}) parts of the fluid-velocity gradient matrix \mathbb{A} : $\omega^2 = \text{Tr} \mathbb{O} \mathbb{O}^T$ and $\sigma^2 = \text{Tr} \mathbb{S} \mathbb{S}^T$. Figure 2 shows the paths to caustic formation obtained by numerical simulation, using a DNS of two-dimensional incompressible turbulence. Our simulations are performed in a periodic box forced at the large scales, in the regime of direct cascade of enstrophy. A drag-friction term ensures steady-state turbulence; see the Supplemental Material (SM) [36] for more details. The path density in Fig. 2 is colour coded, with the highest densities shown in yellow.

Figure 2(a) shows paths to caustic formation in the $Z - \mathcal{A}^2$ plane, where $\mathcal{A}^2 = \sigma^2 - \omega^2 = \text{Tr}(\mathbb{A}^2)$ is the Okubo-Weiss parameter [37, 38] that discerns hyperbolic from elliptic regions in the flow. We see that most paths (yellow regions) that reach a caustic at $Z = -\infty$ pass a large fluid-gradient threshold $\mathcal{A}^2 \approx 0.2$. The solid and dashed lines are explained in our analysis below.

Figure 2(b) shows that typical paths to caustic formation correspond to large strain σ^2 . Vorticity ω^2 , by contrast, remains small for the majority of paths. Figure 2(c) shows the time evolution of σ^2 and ω^2 prior to caustic formation at $t = 0$. We observe that while ω^2 remains small, σ^2 increases sharply, reaches a large value, and then decreases again. The majority of the large strain, however, persists until the caustic is formed, suggesting that caustics preferentially form in regions of large strain. Appealing to optimal-fluctuation theory, our numerical results point towards an optimal path that underlies caustic formation, characterised by small vorticity and a violent strain. Although the spread in our data is quite large at the value of the Stokes number we used, $St = 0.31$, the optimal path leaves a strong mark

in our data, reflected by the yellow streaks in Fig. 2.

We explain our observations using an optimal fluctuation approach. The first step is to analyse the fixed-point structure and the bifurcations of Eq. (2). To this end, we expand the equation of motion (2) for the 2×2 matrix \mathcal{Z} in a basis of matrices generated by the identity matrix \mathbb{I} and

$$\mathbf{e}_1 = \begin{pmatrix} 0 & -1 \\ 1 & 0 \end{pmatrix}, \quad \mathbf{e}_2 = \begin{pmatrix} 0 & 1 \\ 1 & 0 \end{pmatrix}, \quad \mathbf{e}_3 = \begin{pmatrix} 1 & 0 \\ 0 & -1 \end{pmatrix}. \quad (4)$$

This basis is orthogonal with respect to the inner product defined for two matrices \mathbb{M} and \mathbb{N} by $\langle \mathbb{M}, \mathbb{N} \rangle = \frac{1}{2} \text{Tr}[\mathbb{M}\mathbb{N}]$, so that $\langle \mathbf{e}_i, \mathbf{e}_j \rangle = g_{ij} = g^{ij} = \text{diag}(-1, 1, 1)_{ij}$ and $\mathbf{e}_i^\top = \mathbf{e}^i = g^{ij} \mathbf{e}_j$. Here and in the following, we use the Einstein sum convention. We denote the three-vectors corresponding to \mathcal{Z} and \mathbb{A} by $z^i(t) \equiv \langle \mathbf{e}^i, \mathcal{Z}(t) \rangle$ and $A^i(t) \equiv \langle \mathbf{e}^i, \mathbb{A}(t) \rangle$, respectively. This formulation in terms of the Lorentzian metric g_{ij} [39] is convenient because it disentangles the strain and vorticity parts of the fluid-velocity gradients \mathbb{A} . We have $\mathbb{O} = \omega \mathbf{e}_1$, so that $A^1 = \omega$ describes the vorticity. The other components, A^2 and A^3 , describe the strain, $\mathbb{S} = A^2 \mathbf{e}_2 + A^3 \mathbf{e}_3$. Similarity transformations of \mathcal{Z} , $\tilde{\mathcal{Z}} = \mathbb{P}\mathcal{Z}\mathbb{P}^{-1}$ leave \mathcal{Z} invariant, but transform z^i by means of a proper Lorentz transformation, $\tilde{z}^i = \Lambda_j^i z^j$. The same holds for transformations of \mathbb{A} . The matrix Λ which transforms A^i and z^i has the properties $\Lambda^\top \mathbb{g} \Lambda = \mathbb{g}$, and $\det \Lambda = 1$.

Expanding Eq. (2) in the basis (4), we obtain

$$\text{St} \frac{d}{dt} \mathcal{Z} = -\mathcal{Z} - \frac{1}{2} \mathcal{Z}^2 - 2z_i z^i, \quad (5a)$$

$$\text{St} \frac{d}{dt} z^i = -(\mathcal{Z} + 1) z^i + A^i. \quad (5b)$$

As the time derivatives on the left-hand side of Eq. (5) are multiplied by $\text{St} \ll 1$, we expect the dynamics of \mathcal{Z} and z^i to take place in the vicinity of its stable fixed points, if they exist. For $A^i = 0$, we find three fixed points, $\mathcal{Z} = z^i = 0$, $\mathcal{Z} = -2, z^i = 0$, and $\mathcal{Z} = -1, z_i z^i = 1/4$, whose stability is determined by the eigenvalues of the stability matrix of (5). The fixed point $\mathcal{Z} = z^i = 0$ is stable for $A^i = 0$, but a bifurcation occurs at finite A^i , $(\mathcal{Z}, \mathcal{A}^2) = (-1 + 1/\sqrt{2}, 1/8)$, where the fixed point disappears. We conclude that when $\mathcal{A}^2 < 1/8$, the dynamics (5) takes place in the vicinity of the stable fixed point obtained from the implicit equation

$$-\mathcal{Z}(\mathcal{Z}/2 + 1)(\mathcal{Z} + 1)^2 \sim \mathcal{A}^2 = \sigma^2 - \omega^2. \quad (6)$$

When $\mathcal{A}^2 = 2A_i A^i$ exceeds $1/8$, the fixed point ceases to exist, and the nonlinear dynamics (5) drives \mathcal{Z} to negative infinity, forming a caustic. The evolution (6) of the stable fixed point as a function of \mathcal{A}^2 and σ^2 is shown as the solid lines in Figs. 2(a) and 2(b). The fixed points become unstable at the bifurcation point, $(-1 + 1/\sqrt{2}, 1/8)$, (black dots). Hence, for $\mathcal{A}^2 < 1/8$, particle neighbourhoods are stable and are continuously deformed by the fluid-velocity gradients, according to Eq. (6). For $\mathcal{A}^2 > 1/8$, however, the neighbourhoods

become unstable and collapse after a short time. Expanding Eq. (6) for small \mathcal{Z} , one obtains the approximation $\mathcal{Z} \sim -\mathcal{A}^2$ [dashed lines in Figs. 2(a) and 2(b)] used by Maxey [29] to explain the preferential concentration of heavy particles in incompressible turbulence [7, 30]. This approximation fails to describe caustic formation because it predicts that \mathcal{Z} remains finite, and thus leads to the incorrect conclusion that particle neighbourhoods are always stable.

Our stability analysis of Eq. (5) explains the qualitative shape of the paths in Fig. 2(a). However, it misses some of the important results of our DNS. In particular, the stability analysis does not explain why only the strain contributes to caustic formation and vorticity remains small [Fig. 2(b)], and it has no bearing on the time evolution of the large gradient fluctuations shown in Fig. 2(c). Finally, we observed in Fig. 2(a) that the threshold reached by most paths is actually slightly larger than $1/8 = 0.125$, the value predicted by our stability analysis.

In order to explain these parts of our observations we need to go beyond the stability analysis, and consider how the fluid-velocity gradients reach the large threshold required to render particle neighbourhoods unstable. We do this in the following by computing their optimal fluctuation.

The steady-state correlation functions of \mathbb{S} and \mathbb{O} , evaluated along particle trajectories in isotropic and homogeneous turbulence, have the general form

$$\langle S_{ik}(t) S_{jl}(t') \rangle_s = C_{ijkl}^{\mathbb{S}} \langle \text{Tr} \mathbb{S}(t) \mathbb{S}^\top(t') \rangle_s, \quad (7a)$$

$$\langle O_{ik}(t) O_{jl}(t') \rangle_s = C_{ijkl}^{\mathbb{O}} \langle \text{Tr} \mathbb{O}(t) \mathbb{O}^\top(t') \rangle_s, \quad (7b)$$

and $\langle S_{ik}(t) O_{jl}(t') \rangle_s = 0$. In two spatial dimensions, the tensors in Eqs. (7) are given by $C_{ijkl}^{\mathbb{S}} = 1/4(\delta_{ij}\delta_{kl} + \delta_{il}\delta_{jk} - \delta_{ik}\delta_{jl})$ and $C_{ijkl}^{\mathbb{O}} = 1/2(\delta_{ij}\delta_{kl} - \delta_{il}\delta_{jk})$. We express Eqs. (7) in terms of the basis (4) to obtain the steady-state correlations of A^i ,

$$\langle A^1(t) A^1(t') \rangle_s = \frac{1}{2} \langle \text{Tr} \mathbb{O}(t) \mathbb{O}^\top(t') \rangle_s, \quad (8)$$

$$\langle A^2(t) A^2(t') \rangle_s = \langle A^3(t) A^3(t') \rangle_s = \frac{1}{4} \langle \text{Tr} \mathbb{S}(t) \mathbb{S}^\top(t') \rangle_s.$$

All other correlations of A^i are zero in the steady state. The right-hand sides of Eqs. (8) are parametrised as

$$\langle \text{Tr} \mathbb{S}(t) \mathbb{S}^\top(t') \rangle_s = \text{St}^2 C_{\mathbb{S}}(\text{St}) f[(t - t')/s], \quad (9a)$$

$$\langle \text{Tr} \mathbb{O}(t) \mathbb{O}^\top(t') \rangle_s = \text{St}^2 C_{\mathbb{O}}(\text{St}) g[(t - t')/o], \quad (9b)$$

with the non-dimensional correlation times s and o of \mathbb{S} and \mathbb{O} , respectively. For tracer particles with $\text{St} = 0$ one has $C_{\mathbb{S}}(0) = C_{\mathbb{O}}(0) = 1/2$. Inertial particles with $\text{St} > 0$ tend to avoid vortical regions due to preferential concentration [29, 30], so that $C_{\mathbb{O}}(\text{St}) < 1/2$. The amplitude $C_{\mathbb{S}}$, on the other hand, remains approximately equal to $1/2$ [26]. In our two-dimensional numerics, we also find $C_{\mathbb{S}}(\text{St}) \approx 1/2$ for Stokes numbers between 0.21 and 0.51.

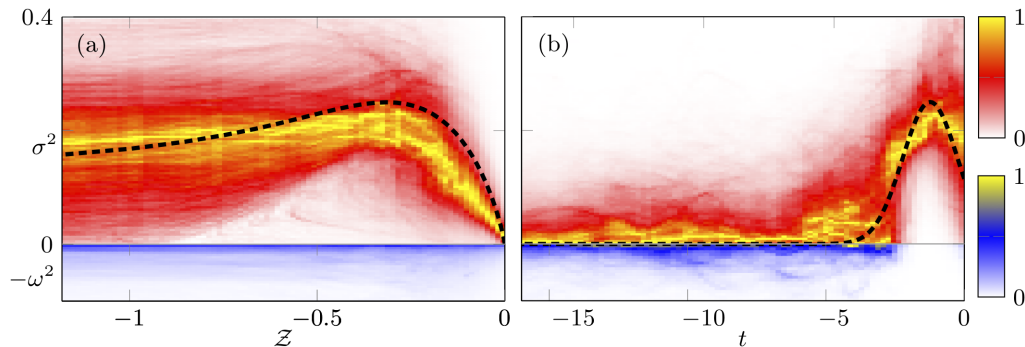


FIG. 3. Optimal paths obtained from theory and path density for $St = 0.31$ from DNS. (a) $(\mathcal{Z}_{\text{opt}}, \sigma_{\text{opt}}^2)$ from theory (dashed line). The colour-coded path density is the same as in Fig. 2(b). (b) $\sigma_{\text{opt}}^2(t)$ from theory (dashed line). The colour-coded path density is the same as in Fig. 2(c).

The functions f and g in Eqs. (9) are normalised to unity, $f(0) = g(0) = 1$. Their time dependencies are well approximated by $f(t) = \exp(-t^2)$ and $g(t) = \exp(-t)$ (see Fig. 1 in the SM [36]).

To describe how the fluid-velocity gradients reach the required threshold values, we model $A^i(t)$ as independent, stationary Gaussian processes with zero mean. For this class of processes, the most probable (optimal) fluctuation $A_{\text{opt}}^i(t)$ to reach a given threshold can be obtained by optimal-fluctuation methods, as we show in the SM [36]. By minimising the action associated with the path probability, we find that the optimal fluctuation of the fluid-velocity gradients is free of vorticity, $\omega_{\text{opt}}^2 = 0$, in agreement with our DNSs in Figs. 2(b) and (c). This result is intuitive: Vorticity contributes to \mathcal{A}^2 with a negative sign, so that any fluctuation of $\mathcal{A}^2 = \sigma^2 - \omega^2$ that reaches the large threshold $\mathcal{A}_{\text{th}}^2$ with finite vorticity requires an even larger strain contribution, to make up for vorticity. The optimal way to reach the threshold value is thus through paths that are vorticity free, whereas the probabilities of paths with finite vorticity are exponentially suppressed. The optimal path for the strain, by contrast, is found to be a time-localised fluctuation, $\sigma_{\text{opt}}^2 = \mathcal{A}_{\text{th}}^2 e^{-2(t-t_{\text{th}})^2/s^2}$, given by a Gaussian function peaked at time $t_{\text{th}} < 0$ [36].

Using the optimal gradient fluctuation $(\sigma_{\text{opt}}^2, \omega_{\text{opt}}^2)$, we now obtain the explicit form for the optimal path $(\mathcal{Z}_{\text{opt}}, \sigma_{\text{opt}}^2)$ as a function of time. For $St \ll 1$, the left-hand sides of Eqs. (5) are small most of the time. To evaluate \mathcal{Z}_{opt} , we therefore use A_{opt}^i as an input into Eq. (5). Making use of the fact that the vorticity is zero along the optimal path, $\omega_{\text{opt}} = 0$, we find that $A_{\text{opt}} = A_{\text{opt}}^i e_i$ and $\mathcal{Z}_{\text{opt}} = 1/2 \mathcal{Z}_{\text{opt}} + z_{\text{opt}}^i e_i$ can be brought into diagonal form by a Lorentz transformation [36]. The equations for the diagonal entries (eigenvalues) $\lambda_{\text{opt}}^{\pm}$ of \mathcal{Z}_{opt} decouple into two equations,

$$\text{St} \frac{d}{dt} \lambda_{\text{opt}}^{\pm} = -\lambda_{\text{opt}}^{\pm} - (\lambda_{\text{opt}}^{\pm})^2 \pm \frac{\mathcal{A}_{\text{th}}}{\sqrt{2}} e^{-(t-t_{\text{th}})^2/s^2}, \quad (10)$$

with initial conditions $\lambda^{\pm}(t_0) = \pm \mathcal{A}_{\text{th}} e^{-(t_0-t_{\text{th}})^2/s^2}/\sqrt{2}$. The uncoupled Eqs. (10) are solved numerically, which

yields the optimal path \mathcal{Z}_{opt} using $\mathcal{Z}_{\text{opt}} = \lambda_{\text{opt}}^+ + \lambda_{\text{opt}}^-$.

We note that for finite St , the threshold value $\mathcal{A}_{\text{th}}^2$, determined numerically [36], exceeds the value $1/8$ obtained from the stability analysis, in agreement with our DNS. The reason is that the optimal strain fluctuation $\sigma_{\text{opt}}^2(t)$ decreases for $t > t_{\text{th}}$. In order for \mathcal{Z}_{opt} to reach negative infinity, $\sigma_{\text{opt}}^2(t)$ must exceed $1/8$ for a finite time so that \mathcal{Z}_{opt} can become large and negative. The time for which the threshold must exceed $1/8$ decreases as St becomes smaller, and we recover $\mathcal{A}^2 \rightarrow 1/8$ in the limit $St \rightarrow 0$.

In Fig. 3, we compare our theory and DNSs. The dashed line in Fig. 3(a) shows $(\mathcal{Z}_{\text{opt}}, \sigma_{\text{opt}}^2)$ obtained from Eqs. (10), with $St = 0.31$ and dimensionless correlation time $s = 2.1$ determined numerically. We observe qualitative agreement between the theoretically obtained optimal path and the (yellow) regions of high path density. However, Eqs. (10) slightly overestimate the threshold value $\mathcal{A}_{\text{th}}^2$. The likely reason is that the Stokes number in our DNS is too large to closely follow our analytical results, valid for $St \ll 1$.

Figure 3(b) shows the time dependence of $\sigma_{\text{opt}}^2(t)$ obtained from theory with $St = 0.31$ (dashed line) and the corresponding path density from our DNS. We observe that the theory correctly predicts the localised, violent fluctuation of the strain prior to the formation of the caustic, which occurs at $t = 0$. A considerable fraction of the large strain required to initialise the caustic persists at the time of caustic formation, which explains why caustics form preferentially in regions of large strain [26, 27]. For other Stokes numbers between 0.24 and 0.51, our DNS results lead to the same conclusion (data not shown).

In conclusion, we explained caustic formation in turbulent aerosols at small particle inertia as an optimal-fluctuation problem. In order for caustics to form, the fluid-velocity gradients must follow an optimal path, characterised by small vorticity and a violent strain that exceeds a large threshold. The remnants of the optimal fluctuation at the time of caustic formation result in a strong instantaneous correlation between large strains

and caustic events.

Since caustics give rise to a multivalued particle-velocity field, and thus to high relative particle velocities, our results provide an explanation for the recently observed, instantaneous correlation between particle collisions and intense strain [26, 27]. The characteristic shape of the optimal path to caustic formation will allow one to identify caustics in experiments, and the strong instantaneous correlation of caustics and strain makes it possible to efficiently sample caustics in simulations.

The stability analysis described in this Letter can be generalised to three dimensions, where it reveals that particle neighbourhoods become unstable when the two invariants $Q = -\text{Tr}A^2/2$ and $R = -\text{Tr}A^3/3$ reach large thresholds in the Q - R plane. We therefore speculate that optimal-fluctuation methods also explain caustic formation in three-dimensional turbulence at small Stokes numbers.

ACKNOWLEDGMENTS

K.G. thanks J. Vollmer for discussions regarding the role of the invariants Q and R for caustic formation in

turbulence. J.M., K.G., and B.M. were supported by the grant *Bottlenecks for particle growth in turbulent aerosols* from the Knut and Alice Wallenberg Foundation, Grant No. KAW 2014.0048, and in part by VR Grant No. 2017-3865. D.M. acknowledges the support of the Swedish Research Council Grant No. 638-2013-9243 as well as Grant No. 2016-05225. V.P. and P.P. acknowledge support from intramural funds at TIFR Hyderabad from the Department of Atomic Energy (DAE), India and DST (India) Project No. ECR/2018/001135. The simulations were performed using resources provided by TIFR, Hyderabad and the Swedish National Infrastructure for Computing (SNIC) at the PDC center for high performance computing.

-
- [1] E. Bodenschatz, S. P. Malinowski, R. A. Shaw, and F. Stratmann, Can we understand clouds without turbulence?, *Science* (80-.). **327**, 970 (2010).
 - [2] A. Johansen, J. Blum, H. Tanaka, C. Ormel, M. Bizzarro, and H. Rickman, The multifaceted planetesimal formation process, *Protostars Planets VI* (2014).
 - [3] M. Wilkinson, B. Mehlig, and V. Uski, Stokes Trapping and Planet Formation, *Astrophys. J. Suppl. Ser.* **176**, 484 (2008).
 - [4] G. Falkovich, K. Gawedzki, and M. Vergassola, Particles and fields in fluid turbulence, *Rev. Mod. Phys.* **73**, 913 (2001).
 - [5] E. Balkovsky, G. Falkovich, and A. Fouxon, Intermittent distribution of inertial particles in turbulent flows, *Phys. Rev. Lett.* **86**, 2790 (2001).
 - [6] J. Bec, L. Biferale, G. Boffetta, M. Cencini, S. Musacchio, and F. Toschi, Lyapunov exponents of heavy particles in turbulence, *Phys. Fluids* **18**, 091702 (2006).
 - [7] K. Gustavsson and B. Mehlig, Statistical models for spatial patterns of heavy particles in turbulence, *Adv. Phys.* **65**, 1 (2016).
 - [8] B. Mehlig and M. Wilkinson, Coagulation by random velocity fields as a Kramers problem, *Phys. Rev. Lett.* **92**, 250602 (2004).
 - [9] M. Wilkinson and B. Mehlig, Caustics in turbulent aerosols, *Europhys. Lett.* **71**, 186 (2005).
 - [10] M. Wilkinson, B. Mehlig, and V. Bezuglyy, Caustic activation of rain showers, *Phys. Rev. Lett.* **97**, 048501 (2006).
 - [11] G. Falkovich, A. Fouxon, and M. Stepanov, Acceleration of rain initiation by cloud turbulence, *Nature* **419**, 151 (2002).
 - [12] G. Falkovich and A. Pumir, Sling Effect in Collisions of Water Droplets in Turbulent Clouds, *J. Atmos. Sci.* **64**, 4497 (2007).
 - [13] K. Gustavsson and B. Mehlig, Distribution of relative velocities in turbulent aerosols, *Phys. Rev. E* **84**, 045304 (2011).
 - [14] K. Gustavsson and B. Mehlig, Relative velocities of inertial particles in turbulent aerosols, *J. Turbul.* **15**, 34 (2014).
 - [15] V. Perrin and H. Jonker, Relative velocity distribution of inertial particles in turbulence - a numerical study, *Phys. Rev. E* **92**, 043022 (2015).
 - [16] A. Bhatnagar, K. Gustavsson, and D. Mitra, Statistics of the relative velocity of particles in turbulent flows: Monodisperse particles, *Phys. Rev. E* **97**, 23105 (2018).
 - [17] S. Sundaram and L. R. Collins, Collision statistics in an isotropic particle-laden turbulent suspension, *J. Fluid Mech.* **335**, 75 (1997).
 - [18] M. Voßkuhle, A. Pumir, E. Lévêque, and M. Wilkinson, Prevalence of the sling effect for enhancing collision rates in turbulent suspensions, *J. Fluid Mech.* **749**, 841 (2014).
 - [19] A. Pumir and M. Wilkinson, Collisional aggregation due to turbulence, *Annu. Rev. Condens. Matter Phys.* **7**, 141 (2016).
 - [20] A. Crisanti, M. Falcioni, A. Provenzale, P. Tanga, and A. Vulpiani, Dynamics of passively advected impurities in simple two-dimensional flow models, *Phys. Fluids A Fluid Dyn.* **4**, 1805 (1992).
 - [21] J. E. Martin and E. Meiburg, The accumulation and dispersion of heavy particles in forced two-dimensional mixing layers. I. The fundamental and subharmonic cases, *Phys. Fluids* **6**, 1116 (1994).
 - [22] J. Bec, A. Celani, M. Cencini, and S. Musacchio, Clustering and collisions of heavy particles in random smooth

- flows, *Phys. Fluids* **17**, 073301 (2005).
- [23] L. Ducasse and A. Pumir, Inertial particle collisions in turbulent synthetic flows: quantifying the sling effect, *Phys. Rev. E* **80**, 66312 (2009).
- [24] K. Gustavsson and B. Mehlig, Distribution of velocity gradients and rate of caustic formation in turbulent aerosols at finite Kubo numbers, *Phys. Rev. E* **87**, 023016 (2013).
- [25] M. W. Reeks, Transport, mixing and agglomeration of particles in turbulent flows, *Flow, Turbul. Combust.* **92**, 3 (2014).
- [26] V. E. Perrin and H. J. J. Jonker, Preferred location of droplet collisions in turbulent flows, *Phys. Rev. E* **89**, 33005 (2014).
- [27] J. R. Picardo, L. Agasthya, R. Govindarajan, and S. S. Ray, Flow structures govern particle collisions in turbulence, *Phys. Rev. Fluids* **4**, 32601 (2019).
- [28] G. P. Bewley, E. W. Saw, and E. Bodenschatz, Observation of the sling effect, *New J. Phys.* **15**, 083051 (2013).
- [29] M. R. Maxey, The gravitational settling of aerosol particles in homogeneous turbulence and random flow fields, *J. Fluid Mech.* **174**, 441 (1987).
- [30] K. D. Squires and J. K. Eaton, Preferential concentration of particles by turbulence, *Phys. Fluids A* **3**, 1169 (1991).
- [31] J. Zittartz and J. S. Langer, Theory of bound states in a random potential, *Phys. Rev.* **148**, 741 (1966).
- [32] A. Eriksson, F. Elías-Wolff, and B. Mehlig, Metapopulation dynamics on the brink of extinction, *Theor. Popul. Biol.* **83**, 101 (2013).
- [33] A. Kamenev, B. Meerson, and B. Shklovskii, How colored environmental noise affects population extinction, *Phys. Rev. Lett.* **101**, 268103 (2008).
- [34] V. Gurarie and A. Migdal, Instantons in the Burgers equation, *Phys. Rev. E* **54**, 4908 (1996).
- [35] J. Bec and K. Khanin, Burgers turbulence, *Phys. Rep.* **447**, 1 (2007).
- [36] Supplemental Material available at ... for details on mathematical derivations and numerical simulations, as well as for numerical results for the correlation functions in Eq. (9). The Supplemental Material also contains Refs. [40–45].
- [37] A. Okubo, Oceanic diffusion diagrams, *Deep Sea Res.* **18**, 789–802 (1971).
- [38] J. Weiss, The dynamics of enstrophy transfer in two-dimensional hydrodynamics, *Phys. D Nonlinear Phenom.* **48**, 273 (1991).
- [39] K. Nomizu and U. Pinkall, Lorentzian geometry for 2x2 real matrices, *Linear Multilinear Algebr.* **28**, 207 (1991).
- [40] T. Grafke, R. Grauer, and T. Schäfer, The instanton method and its numerical implementation in fluid mechanics, *J. Phys. A Math. Theor.* **48**, 333001 (2015).
- [41] N. Van Kampen, *Stochastic Processes in Physics and Chemistry*, (Elsevier, 2007).
- [42] P. C. Martin, E. D. Siggia, and H. A. Rose, Statistical dynamics of classical systems, *Phys. Rev. A* **8**, 423 (1973).
- [43] R. Graham and T. Tél, Existence of a potential for dissipative dynamical systems, *Phys. Rev. Lett.* **52**, 9 (1984).
- [44] A. J. Bray and A. J. McKane, Instanton calculation of the escape rate for activation over a potential barrier driven by colored noise, *Phys. Rev. Lett.* **62**, 493 (1989).
- [45] L. Onsager and S. Machlup, Fluctuations and irreversible processes, *Phys. Rev.* **91**, 1505 (1953).

Supplemental material for ‘Paths to caustic formation in turbulent aerosols’

Jan Meibohm,¹ Vikash Pandey,² Akshay Bhatnagar,³ Kristian Gustavsson,¹ Dhruvaditya Mitra,³ Prasad Perlekar,² and B. Mehlig¹

¹*Department of Physics, Gothenburg University, SE-41296 Gothenburg, Sweden*

²*TIFR Centre for Interdisciplinary Sciences, Tata Institute of Fundamental Research, Gopanally, Hyderabad 500046, India*

³*NORDITA, Royal Institute of Technology and Stockholm University, Roslagstullsbacken 23, SE-10691 Stockholm, Sweden*

In this supplemental material we provide additional details regarding the analytical calculations summarised in the main text, and for the numerical simulations used to obtain the results shown in Figs. 2 and 3 in the main text.

I. INSTANTON CALCULATION FOR THE FLUID-VELOCITY GRADIENTS

In this section we explain in detail the instanton calculation outlined in the main text. We consider the problem of the gradient process A^i reaching a threshold value given by $2A_i A^i = 2(-A_1^2 + A_2^2 + A_3^2) = \mathcal{A}_{\text{th}}$. In particular, we explain how to derive the time dependence of the optimal paths for the gradient processes A_{opt}^i , ω_{opt}^2 and σ_{opt}^2 .

We model the individual components A^i of the fluid-velocity gradient matrix \mathbb{A} by independent, stationary Gaussian processes with zero mean and steady-state correlation functions [cf. Eqs. (8) and (9) in the main text],

$$\begin{aligned} \langle A^1(t)A^1(t') \rangle_s &= \frac{1}{2} \text{St}^2 C_{\text{O}}(\text{St}) g[(t-t')/o], \\ \langle A^2(t)A^2(t') \rangle_s &= \langle A^3(t)A^3(t') \rangle_s = \frac{1}{4} \text{St}^2 C_{\text{S}}(\text{St}) f[(t-t')/s]. \end{aligned} \quad (\text{S1})$$

Figure 1 shows our numerical data for the correlation functions. Figure 1(a) shows that $\langle \text{Tr} \mathbb{O}(t) \mathbb{O}(0) \rangle_s$ is well approximated by a Gaussian function, $f(t) = \exp(-t^2)$. The correlation function of $\mathbb{O}(t)$, shown in Fig. 1(b), is close to an exponential function, so that we choose $g(t) = \exp(-t)$. In Eqs. (S1), o and s are the dedimensionalised correlation times defined in the main text. From the gray line in Fig. 1 we estimate $s \approx 2.1$ for all measured Stokes numbers, while o varies between $o \approx 11$ for $\text{St} = 0.18$ and $o \approx 6$ for $\text{St} = 0.51$.

To obtain the optimal fluctuation to reach a threshold, we consider the transition probability of the gradients A^i from $A^i(t_0) = 0$ at time t_0 , to a large threshold value $A^i(t_{\text{th}}) = a^i$ at time t_{th} . Because the processes A^i are independent, we compute this transition probability for a single process $A(t)$ with arbitrary correlation function. For the Ornstein-Uhlenbeck process, it is well known [1] how to compute the optimal path to reach a threshold. Here we use a similar method, but generalised to any stationary Gaussian process. The processes we consider need not be Markovian as the Ornstein-Uhlenbeck process, and may not have a representation in terms of a stochastic differential equation.

The transition probability of the zero-mean process $A(t)$ from zero at time t_0 , to a at time t_{th} can be written in

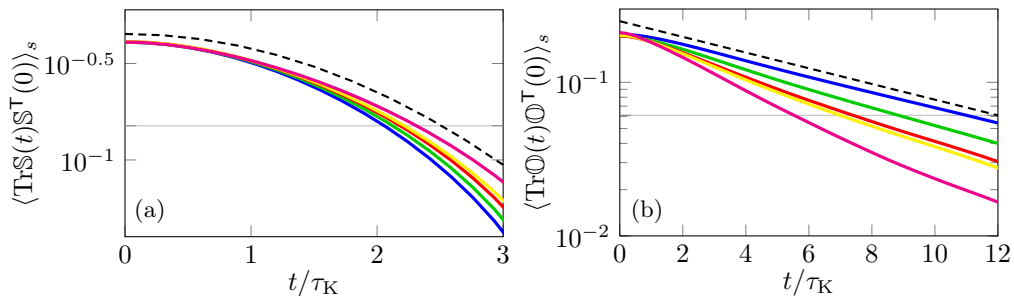


FIG. 1. (a) Steady-state correlation functions for different Stokes numbers, $\text{St} = 0.18$ (blue), 0.24 (green), 0.31 (red), 0.34 (yellow), 0.51 (magenta), as functions of time, measured along heavy-particle trajectories. (a) Correlation function $\langle \text{Tr}[\mathbb{S}(0) \mathbb{S}^T(t)] \rangle_s$. The black dashed line shows a Gaussian function for comparison. The light grey line corresponds to $\approx e^{-1} \times \langle \text{Tr}[\mathbb{S}(0) \mathbb{S}^T(0)] \rangle_s$. (b) Correlation function $\langle \text{Tr}[\mathbb{O}(0) \mathbb{O}^T(t)] \rangle_s$. The black dashed line shows an exponential function for comparison. The light grey line corresponds to $\approx e^{-1} \times \text{Tr}[\mathbb{O}(0) \mathbb{O}^T(0)]_s$.

terms of a path integral

$$P[A(t_{\text{th}}) = a, t_{\text{th}} | A(t_0) = 0, t_0] = \mathcal{N} \int \mathcal{D} \left(\frac{z(t)}{2\pi} \right) \exp \left\{ i \int_{t_0}^{t_{\text{th}}} dt z(t) A(t) \right\} G[z(t)], \quad (\text{S2})$$

where $G[z(t)]$ denotes the generating functional of $A(t)$ and \mathcal{N} is a normalisation factor. For Gaussian processes, $G[z(t)]$ is known explicitly [2]

$$\begin{aligned} G[z(t)] &= \left\langle \exp \left\{ -i \int_{t_0}^{t_{\text{th}}} dt z(t) A(t) \right\} \middle| A(t_{\text{th}}) = a, A(t_0) = 0 \right\rangle, \\ &= \exp \left\{ -\frac{1}{2} \int_{t_0}^{t_{\text{th}}} dt \int_{t_0}^{t_{\text{th}}} dt' z(t) c_{t_0}(t, t') z(t') \right\}. \end{aligned} \quad (\text{S3})$$

Here c_{t_0} is the conditional correlation function of A , defined as

$$c_{t_0}(t, t') = \langle A(t) A(t') | A(t_0) = 0 \rangle. \quad (\text{S4})$$

The conditioning implies $c_{t_0}(t_0, t) = c_{t_0}(t, t_0) = 0$ for all $t \geq t_0$. As $t_0 \rightarrow -\infty$, A becomes stationary, so that

$$\lim_{t_0 \rightarrow -\infty} c_{t_0}(t, t') = c_s(t - t') = \langle A(t) A(t') \rangle_s. \quad (\text{S5})$$

Here $c_s(t - t')$ denotes the steady-state correlation function of $A(t)$ which also defines the variance ε^2 of the process, $c_s(0) = \varepsilon^2$. Using the above expressions, we write Eq. (S2) as

$$P[A(t_{\text{th}}) = a, t_{\text{th}} | A(t_0) = 0, t_0] = \mathcal{N} \int \mathcal{D} \left(\frac{z(t)}{2\pi} \right) e^{-S_{t_0}[z, A]}, \quad (\text{S6})$$

with action $S_{t_0}[z, A]$ given by

$$S_{t_0}[z, A] = -i \int_{t_0}^{t_{\text{th}}} dt z(t) A(t) + \frac{1}{2} \int_{t_0}^{t_{\text{th}}} dt \int_{t_0}^{t_{\text{th}}} dt' z(t) c_{t_0}(t, t') z(t'). \quad (\text{S7})$$

We consider weak-inertia case $\text{St} \ll 1$ which corresponds to $\varepsilon \ll 1$. In this case, the path integration in Eq. (S7) is well-known to concentrate around an ‘optimal path’ $(z_{\text{opt}}, A_{\text{opt}})$ [3, 4]. This path is obtained by a variation of the action $S_{t_0}[z, A]$ over $z(t)$ that vanishes at the optimal path:

$$0 = \delta S_{t_0}[z, A] \Big|_{A=A_{\text{opt}}, z=z_{\text{opt}}} = -i \left\{ \int_{t_0}^{t_{\text{th}}} dt \delta z(t) \left[A_{\text{opt}}(t) + i \int_{t_0}^{t_{\text{th}}} dt' c_{t_0}(t, t') z_{\text{opt}}(t') \right] \right\}. \quad (\text{S8})$$

This determines the optimal path A_{opt} for $A(t)$:

$$A_{\text{opt}}(t) = -i \int_{t_0}^{t_{\text{th}}} dt' c_{t_0}(t, t') z_{\text{opt}}(t'). \quad (\text{S9})$$

The transition probability (S2), and thus the action $S_{t_0}[z, A]$, depends on $A(t)$ only through the final point, $A(t_{\text{th}}) = a$. As a consequence, $z_{\text{opt}}(t)$ has the general form

$$z_{\text{opt}}(t) = iC \delta(t - t_{\text{th}}), \quad \text{which gives,} \quad A_{\text{opt}}(t) = \frac{C}{2} c_{t_0}(t, t_{\text{th}}). \quad (\text{S10})$$

The constant C is evaluated by using the boundary condition $A_{\text{opt}}(t_{\text{th}}) = a$. We find

$$\frac{C}{2} = \frac{a}{c_{t_0}(t_{\text{th}}, t_{\text{th}})}, \quad \text{and thus,} \quad A_{\text{opt}}(t) = \frac{a c_{t_0}(t, t_{\text{th}})}{c_{t_0}(t_{\text{th}}, t_{\text{th}})}. \quad (\text{S11})$$

Upon substituting Eqs. (S11) and (S10) into Eq. (S7), the action $S_{t_0}[z_{\text{opt}}, A_{\text{opt}}]$ evaluated along the optimal path $(z_{\text{opt}}, A_{\text{opt}})$ reads

$$S_{t_0}[z_{\text{opt}}, A_{\text{opt}}] = \frac{1}{2} \frac{a^2}{c_{t_0}(t_{\text{th}}, t_{\text{th}})}. \quad (\text{S12})$$

Minimising $S_{t_0}[z_{\text{opt}}, A_{\text{opt}}]$ over initial times t_0 [1] gives $t_0 \rightarrow -\infty$. This yields for $t \leq t_{\text{th}}$,

$$S[z_{\text{opt}}, A_{\text{opt}}] = \lim_{t_0 \rightarrow -\infty} S_{t_0}[z_{\text{opt}}, A_{\text{opt}}] = \frac{a^2}{2\varepsilon^2}, \quad A_{\text{opt}}(t) = \frac{a c_s(t - t_{\text{th}})}{\varepsilon^2} = \frac{a \langle A(t_{\text{th}})A(t) \rangle_s}{\varepsilon^2}. \quad (\text{S13})$$

For $t > t_{\text{th}}$, the process is unconstrained and relaxes from a to zero as $t \rightarrow \infty$. Unconstrained relaxation does not contribute to the action [5]. Furthermore, for time-reversal invariant processes $A(t)$, the optimal path for the relaxation from the threshold a must be identical to the time-reversed optimal trajectory A_{opt} for reaching the threshold. This argument gives A_{opt} for all t ,

$$A_{\text{opt}}(t) = \frac{a c_s(|t - t_{\text{th}}|)}{\varepsilon^2}. \quad (\text{S14})$$

In other words, for a time-reversible Gaussian, stationary process with zero mean, the optimal path for reaching a threshold a is, up to a constant, given by the steady-state correlation function. The action S depends only on the variance ε^2 , and is otherwise independent of the details of the process $A(t)$. For the Ornstein-Uhlenbeck process, our results agree with those in Ref. [1] based on the Onsager-Machlup action [6].

We now apply Eqs. (S13) and (S14) to the specific, independent processes A^i with steady-state correlation functions (S1) and $f(t) = \exp(-t^2)$ and $g(t) = \exp(-t)$. Comparing Eq. (S14) with (S1) we have $\varepsilon^2 = \frac{1}{2}\text{St}^2 C_{\text{O}}(\text{St})$, $c_s(|t - t_{\text{th}}|)/\varepsilon^2 = g(|t|)$ for A^1 and $\varepsilon^2 = \frac{1}{4}\text{St}^2 C_{\text{S}}(\text{St})$, $c_s(|t - t_{\text{th}}|)/\varepsilon^2 = f(|t|)$ for $A^{2,3}$. Hence,

$$A_{\text{opt}}^1 = a^1 \exp[-|t - t_{\text{th}}|/o], \quad A_{\text{opt}}^{2,3} = a^{2,3} \exp[-(t - t_{\text{th}})^2/s^2], \quad (\text{S15})$$

$$P(a^i, t_{\text{th}}) = \lim_{t_0 \rightarrow -\infty} P[A^i(t_{\text{th}}) = a^i, t_{\text{th}} | A^i(t_0) = 0, t_0] \propto \exp \left\{ -\frac{(a^1)^2}{\text{St}^2 C_{\text{O}}(\text{St})} - \frac{2[(a^2)^2 + (a^3)^2]}{\text{St}^2 C_{\text{S}}(\text{St})} \right\}. \quad (\text{S16})$$

The parameters a^i are obtained by minimising the action $S(a^i)$ in Eq. (S16),

$$S(a^i) = \frac{1}{\text{St}^2} \left\{ \frac{(a^1)^2}{C_{\text{O}}(\text{St})} + \frac{2[(a^2)^2 + (a^3)^2]}{C_{\text{S}}(\text{St})} \right\}, \quad (\text{S17})$$

over all a^1 , a^2 and a^3 subject to the constraint $2a_i a^i = \mathcal{A}_{\text{th}}^2$. This gives $a^1 = 0$, $2[(a^2)^2 + (a^3)^2] = \mathcal{A}_{\text{th}}^2$ with minimal action

$$S = \min_{a^i: 2a_i a^i = \mathcal{A}_{\text{th}}^2} S(a^i) = \mathcal{A}_{\text{th}}^2 / [\text{St}^2 C_{\text{S}}(\text{St})]. \quad (\text{S18})$$

From this result, we obtain

$$\omega_{\text{opt}}^2(t) = 0 \quad \text{and} \quad \sigma_{\text{opt}}^2(t) = 2[(A_{\text{opt}}^2)^2 + (A_{\text{opt}}^3)^2] = \mathcal{A}_{\text{th}}^2 e^{-2(t-t_{\text{th}})^2/s^2}, \quad (\text{S19})$$

as stated in the main text.

II. SOLUTION TO THE EIGENVALUE EQUATIONS FOR \mathbb{Z}

We now show how we obtain our solutions for the optimal path for $\mathcal{Z} = \text{Tr}\mathbb{Z} = \lambda^+ + \lambda^-$ for small $\text{St} \ll 1$ [see main text below Eq. (10)]. We first explain how to derive Eq. (10) in the main text. We then briefly discuss our numerical method to determine the threshold value $\mathcal{A}_{\text{th}}^2$, and to produce Fig. (3) in the main text. To this end, we write

$$\text{St} \frac{d}{dt} \mathcal{Z}_{\text{opt}} = -\mathcal{Z}_{\text{opt}} - \frac{1}{2} \mathcal{Z}_{\text{opt}}^2 - 2(z_{\text{opt}})_i z_{\text{opt}}^i, \quad (\text{S20a})$$

$$\text{St} \frac{d}{dt} z_{\text{opt}}^1 = -(\mathcal{Z}_{\text{opt}} + 1) z_{\text{opt}}^1, \quad (\text{S20b})$$

$$\text{St} \frac{d}{dt} z_{\text{opt}}^2 = -(\mathcal{Z}_{\text{opt}} + 1) z_{\text{opt}}^2 + a^2 e^{-(t-t_{\text{th}})^2/s^2}, \quad (\text{S20c})$$

$$\text{St} \frac{d}{dt} z_{\text{opt}}^3 = -(\mathcal{Z}_{\text{opt}} + 1) z_{\text{opt}}^3 + a^3 e^{-(t-t_{\text{th}})^2/s^2}. \quad (\text{S20d})$$

At time $t = t_0$ we have $\mathbb{Z}(t_0) = \mathbb{A}(t_0)$, so that $\mathcal{Z}_{\text{opt}}(t_0) = 0$. We conclude that $z_{\text{opt}}^1(t) = 0$ for all times. Now, we perform a Lorentz transform, which in this case is just a simple rotation, of the remaining components A_{opt}^2 and

N	f_0	k_f	μ	ν	Re	N_p	St	Θ
1024	5×10^{-3}	4	10^{-2}	10^{-5}	1700	10^5	0.18	-0.51 10

TABLE I. The parameters used in our DNS of two-dimensional turbulence. For the numerical evolution we use a time step of 5×10^{-3} units and a total simulation time of 400 units. The Kolmogorov time evaluates to $\tau_K \approx 2.9$ units.

A_{opt}^3 so that $\tilde{A}_{\text{opt}}^2 = 0$ and $\tilde{A}_{\text{opt}}^3 = \sqrt{(a^2)^2 + (a^3)^2} e^{-(t-t_{\text{th}})^2/s^2} = \mathcal{A}_{\text{th}} e^{-(t-t_{\text{th}})^2/s^2} / \sqrt{2}$. This leaves the general form of Eqs. (S20) invariant, so that we obtain after the transform

$$\text{St} \frac{d}{dt} \mathcal{Z}_{\text{opt}} = -\mathcal{Z}_{\text{opt}} - \frac{1}{2} \mathcal{Z}_{\text{opt}}^2 - 2(\tilde{z}_{\text{opt}})_i \tilde{z}_{\text{opt}}^i, \quad (\text{S21a})$$

$$\text{St} \frac{d}{dt} \tilde{z}_{\text{opt}}^2 = -(\mathcal{Z}_{\text{opt}} + 1) \tilde{z}_{\text{opt}}^2, \quad (\text{S21b})$$

$$\text{St} \frac{d}{dt} \tilde{z}_{\text{opt}}^3 = -(\mathcal{Z}_{\text{opt}} + 1) \tilde{z}_{\text{opt}}^3 + \frac{\mathcal{A}_{\text{th}}}{\sqrt{2}} e^{-(t-t_{\text{th}})^2/s^2}. \quad (\text{S21c})$$

From $\tilde{\mathbb{Z}}(t_0) = \tilde{\mathbb{A}}(t_0)$ we again conclude $\tilde{z}_{\text{opt}}^2(t) = 0$ for all times. Using the initial decomposition we obtain $\tilde{\mathbb{Z}}_{\text{opt}} = \mathcal{Z}_{\text{opt}}/2\mathbb{I} + \tilde{z}^3 \mathbf{e}_3$, where \mathbf{e}_3 is diagonal with elements $\mathbf{e}_3 = \text{diag}(1, -1)$. Hence, we find that after the transformation, $\tilde{\mathbb{Z}}_{\text{opt}}$ is in diagonal form with eigenvalues $\lambda_{\text{opt}}^+ = \mathcal{Z}_{\text{opt}}/2 + \tilde{z}_{\text{opt}}^3$ and $\lambda_{\text{opt}}^- = \mathcal{Z}_{\text{opt}}/2 - \tilde{z}_{\text{opt}}^3$. Taking time-derivatives of these eigenvalues, and using Eqs. (S21), we obtain the uncoupled equations for the eigenvalues λ_{opt}^+ and λ_{opt}^- ,

$$\text{St} \frac{d}{dt} \lambda_{\text{opt}}^+ = -\lambda_{\text{opt}}^+ - (\lambda_{\text{opt}}^+)^2 + \frac{\mathcal{A}_{\text{th}}}{\sqrt{2}} e^{-(t-t_{\text{th}})^2/s^2}, \quad (\text{S22a})$$

$$\text{St} \frac{d}{dt} \lambda_{\text{opt}}^- = -\lambda_{\text{opt}}^- - (\lambda_{\text{opt}}^-)^2 - \frac{\mathcal{A}_{\text{th}}}{\sqrt{2}} e^{-(t-t_{\text{th}})^2/s^2}, \quad (\text{S22b})$$

presented in Eq. (10) in the main text. As the trace of a matrix is the sum of its eigenvalues, we have $\mathcal{Z}_{\text{opt}} = \text{Tr} \mathbb{Z}_{\text{opt}} = \lambda_{\text{opt}}^+ + \lambda_{\text{opt}}^-$. These equations need to be solved numerically with the initial conditions $\lambda_{\text{opt}}^+(t_0) = \frac{\mathcal{A}_{\text{th}}}{\sqrt{2}} e^{-(t_0-t_{\text{th}})^2/s^2}$ and $\lambda_{\text{opt}}^-(t_0) = -\frac{\mathcal{A}_{\text{th}}}{\sqrt{2}} e^{-(t_0-t_{\text{th}})^2/s^2}$.

To determine the threshold value \mathcal{A}_{th} , we start at $\mathcal{A}_{\text{th}} = 1/8$ and increase \mathcal{A}_{th} incrementally until λ_{opt}^- escapes to negative infinity. By returning to the previous \mathcal{A}_{th} , and reducing the step size, we obtain an iterative approximation of the smallest value \mathcal{A}_{th} for which $\lambda_{\text{opt}}^- \rightarrow -\infty$.

When computing the optimal trajectories shown in Fig. (3) in the main text, the threshold value \mathcal{A}_{th} must be exceeded slightly, in order to enable λ^- to escape to negative infinity in finite time. The amount by which the threshold is exceeded is a free parameter in our model. Motivated by the fact that Gaussian fluctuations around the optimal path A_{opt}^i are of the order of the square-root of the variance $(\text{St}^2 C_s(\text{St})/4)^{1/2}$, determined by the action (S17), we choose this parameter equal to $\text{St}/(2\sqrt{2})$. We have checked that our results are insensitive to small changes of this parameter value.

III. DIRECT NUMERICAL SIMULATIONS

In this section, we provide some details of the numerical method we used to solve the two-dimensional Navier-Stokes equations and the particle dynamics, resulting in Figs. 2 and 3 in the letter.

In two spatial dimensions, the incompressible Navier-Stokes equations are conveniently expressed in terms of a stream function $\psi(\mathbf{x}, t)$ and the fluid vorticity $\omega(\mathbf{x}, t) = \nabla \times \mathbf{u}(\mathbf{x}, t)$. Using the stream function ψ , defined by $\mathbf{u} = (-\partial_{x_2} \psi, \partial_{x_1} \psi)$, enforces the incompressibility condition $\nabla \cdot \mathbf{u} = 0$. In terms of ψ and $\omega = \Delta \psi$, the two-dimensional Navier-Stokes equations read

$$\partial_t \omega + \partial_{x_1} \psi \partial_{x_2} \omega - \partial_{x_1} \omega \partial_{x_2} \psi = \nu \nabla^2 \omega - \mu \omega + f. \quad (\text{S23})$$

Here f is a large-scale forcing that generates the turbulence. We take this forcing to be deterministic and time-independent, $f(\mathbf{x}, t) = f_0 \sin(k_f x_2)$. The friction term $-\mu \omega$ in Eq. (S23) ensures a stationary turbulent state. The simulation domain is a square box of side length $L = 2\pi$ with periodic boundary conditions and we discretise the spatial coordinates at N^2 points.

We evolve a large number N_p of particle trajectories by solving simultaneously the Navier-Stokes equation (S23), the single-particle dynamics (1), and, along each particle trajectory, the evolution equation (3) for the particle-velocity gradients \mathbb{Z} . Whenever \mathcal{Z} exceeds a large negative threshold Θ , we record the formation of a caustic. All simulation parameters are summarised in Table I.

-
- [1] T. Grafke, R. Grauer, and T. Schäfer, The instanton method and its numerical implementation in fluid mechanics, *J. Phys. A Math. Theor.* **48**, 333001 (2015).
 - [2] N. Van Kampen, *Stochastic Processes in Physics and Chemistry*, (Elsevier, 2007).
 - [3] P. C. Martin, E. D. Siggia, and H. A. Rose, Statistical dynamics of classical systems, *Phys. Rev. A* **8**, 423 (1973).
 - [4] R. Graham and T. Tél, Existence of a potential for dissipative dynamical systems, *Phys. Rev. Lett.* **52**, 9 (1984).
 - [5] A. J. Bray and A. J. McKane, Instanton calculation of the escape rate for activation over a potential barrier driven by colored noise, *Phys. Rev. Lett.* **62**, 493 (1989).
 - [6] L. Onsager and S. Machlup, Fluctuations and irreversible processes, *Phys. Rev.* **91**, 1505 (1953).